Mechanics Research Communications 122 (2022) 103890

Contents lists available at ScienceDirect

Mechanics Research Communications

journal homepage: www.elsevier.com/locate/mechrescom

Peridynamic modeling of stochastic fractures in bolted glass plates

Fan ZHU [a], Jidong ZHAO [a,*], Roberto BALLARINI [b], Shitao PENG [c], Suwen CHEN [c,d]

[a] Department of Civil & Environmental Engineering, The Hong Kong University of Science and Technology, Clearwater Bay, HKSAR, China
[b] Department of Civil and Environmental Engineering, Cullen College of Engineering, University of Houston, Houston, TX, USA
[c] College of Civil Engineering, Tongji University, Shanghai, China
[d] State Key Laboratory of Disaster Reduction in Civil Engineering, Tongji University, Shanghai, China

ARTICLE INFO

Keywords:
Peridynamics
Glass fracture
Bolt connection
Flaw
Strength statistics

ABSTRACT

This paper presents a peridynamics-based computational approach for modeling fractures in bolted glass plates that features an explicit consideration of randomly distributed micro-flaws. The glass fabrication procedures are assumed to produce a stochastic distribution of a single population of Pareto-distributed surface flaws and mono-sized edge flaws. Numerical simulations are presented of the cracking that develops for varying geometrical configurations of the glass plates under in-plane loads, using a plane stress ordinary state-based peridynamics formulation. The fracture patterns and failure loads predicted by the models agree reasonably well with corresponding experimental observations. The results from a series of simulations suggest that the distribution of strength can be fitted by the Weibull distribution or normal distribution, but is strongly dependent on the assumed values of edge flaw density and flaw depth.

1. Introduction

The use of load-bearing architectural elements made of glass has gained increasing popularity in the past decades, particularly in façade structures. The glass components are designed to resist various types of loads including those associated with wind, snow, impact, vibration, and thermal effects. Determination of the appropriate strength is a critical task for design, because past studies have made it abundantly clear that the strength of glass is highly uncertain and is dependent on a variety of factors associated with its production, transportation, and handling. The ambient service environment, such as temperature and humidity, is also known to degrade glass strength through subcritical crack propagation referred to as static fatigue [1–3]. The presence of randomly distributed surface flaws is generally accepted as a dominating factor to the statistical nature of glass strength, and numerous statistical strength models have been proposed to provide a theoretical basis for engineering design. It is most common to assume that the failure probability of a glass plate follows the Weibull distribution [4], which can be derived from stochastic distribution of either volume or surface flaws [5,6]. Experimental strength data has shown that the traditional two-parameter Weibull model, which assumes a lower bound strength equal to zero and non-interacting cracks, is severely limited in characterizing the strength distribution of glass. The three-parameter Weibull model [7,8] was therefore proposed by considering a lower bound of the glass strength, while bimodal Weibull statistics [9] was proposed to account for the bimodality of the failure probability curve observed in experiments [10]. The glass failure prediction model (GFPM) [11] offers a link between the Weibull failure probability equation [4] with the stress condition in glass with consideration of various factors such as flaw orientation and stress duration.

When bolted connections are used to transfer load between two glass panels or between a glass panel and another structural component, the holes introduced in the glass to accommodate the bolt produce stress concentrations. Therefore, extra care must be taken to ensure adequate strength at the glass-bolt connections. The strength of such connections is known to be strongly dependent on the method used to cut the holes. For instance, the holes drilled by a waterjet generally have the lowest capacity as compared with other cutting methods [12,13]. Measurements of micro-crack sizes using confocal microscopy have further revealed that different edge finishing procedures result in largely different depths and sizes of edge flaws [14], which together with surface flaws (the upper and lower surfaces of the glass panels), dictate the load-bearing capacity of bolted glass connections.

The stochastic behavior of glass strength can also be quantified through micromechanics based computational approaches. These can generally be classified into two categories – the elemental strength

* Corresponding author.
E-mail address: jzhao@ust.hk (J. ZHAO).

https://doi.org/10.1016/j.mechrescom.2022.103890
Received 24 November 2021; Received in revised form 22 March 2022; Accepted 26 March 2022
Available online 27 March 2022

approach and the flaw size approach [15]. The former considers a stochastic distribution of strength of elements in a material domain [16, 17]. It does not directly model the size or orientation of flaws and considers the strength in each element to be isotropic. For the model to be valid, the flaws must be randomly orientated. The elemental strength model may be regarded as an indirect description of the stochastic distribution of discrete flaws. In contrast, the flaw size approach explicitly models discrete and non-interacting surface flaws of randomly distributed size [18–21]. When implemented in Finite Element Method (FEM) analyses, the strength of an element is determined by the largest flaw within it, and according to the weakest-link principle, the material fails when the weakest element does. The flaw size approach has gained popularity with improved computing power that allows Monte Carlo simulations of various scenarios of glass failure [19,21]. An advantage of explicitly modeling the stochastic distribution of flaws is that the physical origin of the glass strength variation can be directly quantified. However, in most existing studies, although the flaws are explicitly considered, the fracture initiation and propagation in the material have not been properly considered. Instead, the material failure is considered through a stress-based criterion where the critical stress is inferred from the Griffith theory. The challenges in modeling material fractures arise from the difficulties in modeling the continuum-discrete transition using traditional methods such as FEM where the partial differential equations cannot be solved in the presence of large numbers of growing and interacting flaws (i.e., discontinuities). The recent development of novel particle-based computational methods offers potential alternatives to the FEM. Notably, the peridynamics (PD) theory, which is a reformulation of continuum mechanics in non-local form [22,23], offers promise for modeling discontinuities and the continuum-discrete transition. The governing equation in PD is formulated in an integral form that can naturally incorporate complex geometric discontinuities. Therefore, the flaw size approach described above can be embedded in a PD model to simulate fracture in glass with the benefit that the initiation and propagation of flaws can be explicitly modeled. In this way, the numerical model can fully capture the physics underlying the macroscopic strength variation without having to resort to phenomenological laws.

In this paper, we employ the PD theory to model fracture and strength statistics of bolted glass panels subjected to in-plane loads. The surface flaws and the edge flaws are incorporated statistically. The failure loads and fracture patterns obtained from simulation are compared with experimental records. This paper is organized as follows. Section 2 presents the methodologies used for the model, including the PD theory, a contact model that accounts for the interaction between the bolt and the glass plate, and statistical models of flaws. Section 3 presents the numerical simulations and validations. The results are summarized in Section 4.

2. Methodology

2.1. Peridynamic theory

The PD theory is an alternative formulation of classical continuum mechanics, in which a continuum material domain is modeled with interactive material points. Several types of PD formulations have been developed to define the interaction between material points. The early-stage PD theory, which is *bond-based*, assumes that material points interact through independent elastic bonds. The formulation is restricted to specific values of the Poisson ratio: 1/3 and 1/4 for 2D and 3D models, respectively. The *state-based* PD (SBPD) formulation lifted the restriction on Poisson ratio by allowing a material bond to depend on neighboring bonds. The SBPD can be further classified into ordinary and non-ordinary types. The former is a pure PD formulation and the latter recasts the PD formulation within the traditional continuum mechanics framework so that classical constitutive models of complex material behavior can be conveniently incorporated within it [23]. For this study, the ordinary SBPD has been employed for modeling the elastic and brittle behaviors of glass. The governing equation can be expressed by

$$\rho_x \ddot{\boldsymbol{u}}_x = \int_{\Omega_x} [\boldsymbol{T}<\boldsymbol{x}'-\boldsymbol{x}> - \boldsymbol{T}<\boldsymbol{x}-\boldsymbol{x}'>]dV_{x'} + \boldsymbol{b}_x \tag{1}$$

where ρ is material density, $\boldsymbol{u}$ denotes deformation, Ω defines the *family* of a point and $V_{x'}$ represents the volume of a neighboring point. The *family* of a material point is defined by a radius named *horizon*. All points within the *horizon* are considered within the *family* of a material point. The *horizon* is taken to be three times the element size in this study. The element size refers to the size of a cube (square for 2D) having the same volume (area for 2D) as the material point. As will be mentioned subsequently, an adaptive scheme for the element size is used in this study to reduce computational cost. Consequently, each point has a specific *horizon* and *family*. The formulation is referred to as dual-horizon PD formulation for which the conservation of linear and angular momentum has been proved [24]. $\boldsymbol{b}$ represents body force density. The subscript denotes a material point and the angled brackets denote a bond vector. $\boldsymbol{T}$ is a force state that maps the bond deformation into bond force density. In the present study we adopt the linear peridynamic solid (LPS) model [23] to simulate glass in plane stress conditions. The force state $\boldsymbol{T}$ is defined following [25] by

$$\boldsymbol{T}<\boldsymbol{x}'-\boldsymbol{x}>= t\frac{\boldsymbol{Y}}{\|\boldsymbol{Y}\|} \tag{2}$$

$$t = \frac{2k'\vartheta}{m}\omega<\|\boldsymbol{\xi}\|>\|\boldsymbol{\xi}\| + \frac{8\mu}{m}\omega<\|\boldsymbol{\xi}\|> \underline{e}^d \tag{3}$$

where $\boldsymbol{\xi}$ and $\boldsymbol{Y}$ represent the undeformed and deformed bond vectors, respectively and t is a scalar force state representing the magnitude of the bond force density. $\boldsymbol{x}' - \boldsymbol{x}$ in the angle brackets denotes the vector originating from point $\boldsymbol{x}$ and pointing to a neighbor point $\boldsymbol{x}'$. These concepts are illustrated in **Fig. 1**. $\omega\langle||\boldsymbol{\xi}||\rangle$ is an influence function computed at bond $\boldsymbol{\xi}$. The influence function is defined to be $\omega\langle||\boldsymbol{\xi}||\rangle = \delta/||\boldsymbol{\xi}||$ in the present study. μ denotes the shear modulus of the glass and $k' = E/2(1-\nu)$ represents the equivalent bulk modulus for plane stress condition where E and ν are the Young's modulus and Poisson ratio, respectively (refer to [26]). The weighted volume m and dilatation ϑ at a material point are computed by

$$m_x = \int_{\Omega_x} \omega<\|\boldsymbol{\xi}\|>\|\boldsymbol{\xi}\|^2\, dV_{x'} \tag{4}$$

$$\vartheta_x = \frac{2}{m_x}\int_{\Omega_x} \omega<\|\boldsymbol{\xi}\|>\|\boldsymbol{\xi}\|\, \underline{e}\, dV_{x'} \tag{5}$$

where $\underline{e} = \|\boldsymbol{Y}\| - \|\boldsymbol{\xi}\|$ represents extension of a bond. It can be further divided into an isotropic part, $\underline{e}^i$, and a deviatoric part $\underline{e}^d$ where $\underline{e}^i = \vartheta\|\boldsymbol{\xi}\|/2$ and $\underline{e}^d = \underline{e} - \underline{e}^i$.

The initiation and propagation of cracks are modeled by allowing the peridynamic bonds to break irreversibly. Once a bond is broken, the load that was originally borne on that bond is redistributed to neighboring bonds and such process may trigger additional breakage of peridynamic

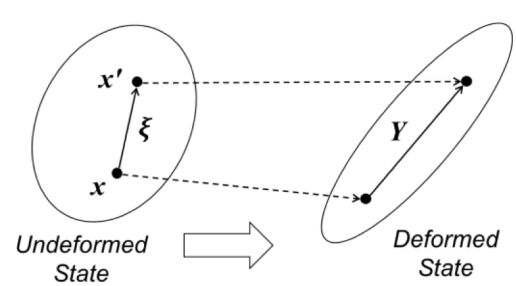

Fig. 1. Schematic illustration of peridynamic bonds.

bonds; thus cracks can initiate and propagate. For elastic brittle materials modeled in this study, a critical stretch damage model [27,28] is employed to simulate bond breakage. The model assumes that a bond breaks when its strain reaches a critical value. The critical bond strain can be related to critical energy release rate of the material through

$$s_c = \sqrt{G_c \Big/ \left\{ \left[\frac{6}{\pi}\mu + \frac{16}{9\pi^2}(k' - 2\mu) \right] \delta \right\}} \tag{6}$$

where G_c is a material constant representing the critical energy release rate. For mode I fracture, G_c is related to the fracture toughness K_c by $G_c = K_c^2/E$. The critical stretch is not a constant in the present study due to the varied element size (and subsequently the varied horizon) adopted. Bonds originating from a material point will have their critical stretch calculated based on the horizon at that point. In the framework of peridynamics, the damage of a material point can be expressed by a weighted percentage of broken bonds as

$$\varphi = 1 - \frac{\int_{\Omega_x} g < \boldsymbol{\xi} > dV_{x'}}{\int_{\Omega_x} dV_{x'}} \tag{7}$$

where $g\langle\boldsymbol{\xi}\rangle$ indicates the status of a bond. If $g\langle\boldsymbol{\xi}\rangle$ is equal to unity the bond is intact, and when it is equal to zero it is broken. Therefore, the damage φ equals zero for an intact material point and rises to a maximum value of 1.0 when all the connecting bonds are broken. The damage parameter of material points is used to locate fracture surfaces.

2.2. Contact model

At the bolt connections, a metal ring is inserted between the bolt and the hole cut in the glass. An elastic contact model is used to model the interactions between the ring and the glass. The contact model has a similar form to the short-range force model used in previous PD studies [29,30] which writes

$$f_c = \min\{0,\ k_n(\| \boldsymbol{Y} \| - d_c)\} \frac{\boldsymbol{Y}}{\| \boldsymbol{Y} \|} \tag{8}$$

where the computed contact force $\boldsymbol{f_c}$ is added into the momentum equation, i.e., Eq. (1), d_c represents a critical distance below which the two points are considered in contact (set equal to the element size). k_n denotes the stiffness at contact which is selected to be 30 N/mm in the present study. In this study, the contact model is mainly used to transfer the loads from the metal ring to the glass panel. It was found that the magnitude of the stiffness does not significantly influence the failure load and fracture patterns of the glass plates. Nonetheless, the stiffness should not be selected too high since this may lead to numerical stability issues. It should also not be chosen too small because this may cause overlapping of contacting material points. Moreover, one should be aware that the contact stiffness may affect material strength if fracture is initiated from the contact region, which, however, is not the case in the present study. It can be inferred from Eq. (8) that the contact force always acts along the bond direction as a repulsive force. The applied contact model is a local model where the material interacts with its immediate surrounding points. Non-local type contact models [31] are also worth future investigation to test their performance when used in the non-local PD framework.

2.3. Surface and edge flaws

The variation in the strength of glass is predominantly attributed to the stochastic distribution of surface flaws. It has been derived that a Pareto distribution in the size of surface flaws leads to a Weibull distribution of strength [32], with evidence that the surface flaw sizes can indeed be described with a Pareto-like distribution [33,34]. Kinsella & Persson [21] further employed a dual-population model for surface flaws to account for the bimodality in glass strength where the large and small flaws are modeled with Pareto and Fréchet distributions, respectively. In the present study, we consider a Pareto distributed population of surface flaws whose cumulative distribution follows

$$P_{(x)} = 1 - \left(\frac{a}{x}\right)^c \tag{9}$$

where $P_{(x)}$ represents the cumulative probability of a flaw with size equal or less than x. The scale parameter a and the shape parameter c are taken to be 0.01 (mm) and 2.0, respectively with reference to [15]. The surface flaw density is assumed to be 2 per cm^2 as suggested by optical measurements [35] for flaw size not less than 8 μm. Surface flaws with size of 200, 150, 100, 50, and 20 μm are assumed. The largest flaw size of 200 μm is adopted from past works [19]. Flaws smaller than 20 μm are not explicitly modeled in view that the discretization adopted in the PD model does not offer such resolution. The flaws are rendered independent of each other by partitioning the material domain into square units with size of 1 cm^2 and inserting them at random positions and extending them at a random direction within each unit.

The flaws at the edges of glass panels are known to be strongly dependent of the machining process. Existing studies show that the flaw size ranges from tens of microns to over 100 microns and can be described by a normal distribution [14]. The edge flaws are modeled at the outer edge and near the holes in the glass panel, and their density is assumed to be the same as that of the surface flaws. The edge flaws are perpendicular to the edge. In the PD model, each flaw is modeled as a pre-existing crack by setting as broken, at the beginning of the analysis, a portion of bonds crossing the crack (which we denote as p) [36]. The parameter p ranges between zero and unity for all cracks and an assumed $p = 1.0$ implies a cut-through crack in the glass. In the simulations, it has been assumed that $p = 0.3$ for all surface flaws and $p = 0.1$ for all edge flaws. p can be generally treated as a numerical parameter that depends on the depth of the flaw. For the edge flaws at the bolt hole, assuming $p = 0.1$ may be roughly interpreted as a flaw with depth of 0.1 times the element size (0.2 mm in this study) thus a flaw depth of 20 microns. The parameter can of course be further calibrated and correlated with different types of flaws.

3. Modeling fractures in bolted glass

3.1. Model setup

Numerical models are created to study the fracture of bolted glass panels under in-plane loads. The scenarios studied include single-bolt connection with varying bolt-to-end and bolt-to-edge distances, and multi-bolt connection with varying hole distance. Fig. 2 shows a schematic illustration of the simulated glass specimens. The length and width of the specimen are 400 mm and 150 mm, respectively, with a thickness of 10 mm. The holes have a diameter of 30 mm. An aluminum ring is positioned inside the hole to host the bolt. Three series of simulations are carried out for the specimen as summarized in Table 1. The first series, denoted by "*E*", deals with varying bolt-to-end distance with

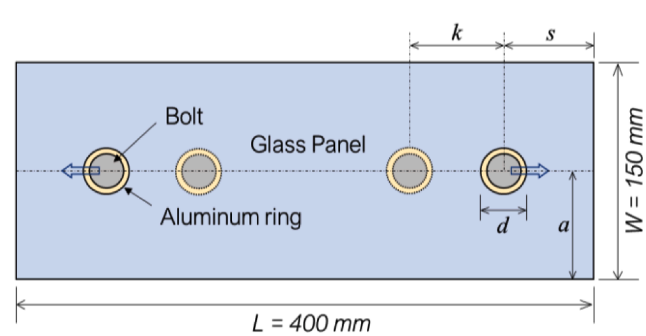

Fig. 2. Schematic illustration of the studied glass specimen.

Table 1
Geometrical configurations of the numerical models.

Case	s/d	a/d	k/d	Case	s/d	a/d	k/d
Base	2.0	2.5	-	*S-2*	2.0	1.5	-
E-1	0.75	2.5	-	*S-3*	2.0	2.0	-
E-2	1.0	2.5	-	*M-1*	2.0	2.5	1.5
E-3	1.5	2.5	-	*M-2*	2.0	2.5	2.0
S-1	2.0	1.0	-	*M-3*	2.0	2.5	3.0

the ratio s/d varying from 0.75 to 2.0. The second series, as denoted by "*S*", models glass fracture with different side distances and the ratio of a/d varies from 1.0 to 2.0. The last series, as denoted by "*M*", investigates multi-bolt connections with different hole spacing. For each case, 20 simulations are performed where the flaws are generated following statistical distributions.

The numerical simulations have been set up according to the pulling tests performed at Tongji University [37], China on ultra-clear glass panels with bolt connections [37]. A total of 61 specimens sharing the same geometrical configurations as listed in Table 1 were tested. From the tests, the bolt-to-end distance *s*, the bolt-to-side distance *a*, the hole spacing *k* as well as the gap between the bolt and the aluminum ring are found to be the key parameters affecting the fracture pattern and the bearing capacity of the glass panels. In the present study, the simulation results are compared with the experimental records for validation purpose.

The properties of the glass used in numerical models are summarized in **Table 2**. For the soda-lime glasses, the toughness typically ranges at 0.72~0.82 MPa•m$^{1/2}$ [38] for mode I fractures. The range of Young's modulus and Poisson ratio are found to be 70~74 GPa and 0.22~0.23, respectively [15,38]. The adopted values therefore reflect typical glass properties. The aluminum ring is assumed to have a density of 2,700 kg/m^3, a Young's modulus of 70 GPa and a Poisson ratio of 0.33.

Setup of the numerical model is illustrated in **Fig. 3**. In view of the symmetrical features of the specimen, in the numerical model we only consider half of the specimen with a boundary condition applied at the original mid-length restricting the displacement along the longitudinal direction. The specimen is discretized into elements with size ranging from 0.2 mm to 1.0 mm, where finer discretization is adopted around the hole and coarse discretization near the edges. Using a fine discretization around the hole is necessary since fractures are expected to initiate from that region and the edge flaws can be modeled more accurately. On the other hand, a fine discretization also mitigates the surface weakening effect in ordinary SBPD [39], improving the accuracy of simulation. Adopting a varying element size can significantly reduce computational cost while maintaining the simulation accuracy. The total number of material points modeled in the different cases ranges from 57,000 to 121,000. It is important to discretize the domain adapting to the specimen geometry especially near the hole area. In this study we use the open-source FEM mesh generator *Gmsh* [40] for the discretization. The mesh was then converted to discretized points by assigning a material point at the centroid of each element which carries the corresponding element area.

Load is applied by applying a constant rate of displacement to the metal ring. It is assumed that the response is quasi-static. A parametric study was performed to determine the maximum displacement rate that does not introduce apparent inertial effects. It was found that the failure load remains practically constant with a loading rate up to 0.4~0.5 m/s.

Table 2
Properties of the glass used in simulation.

Property	Unit	Value
Density	kg/m^3	2,500
Young's modulus	GPa	70
Poisson ratio	-	0.23
Fracture toughness	MPa•m$^{1/2}$	0.8

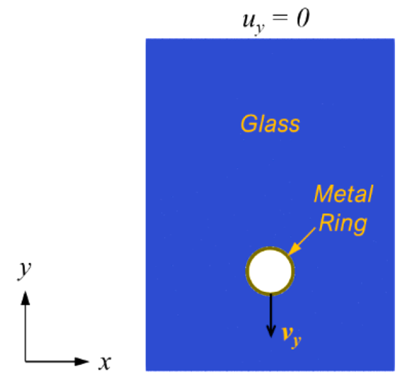

Fig. 3. Schematic illustration of the numerical model setup.

Therefore, a displacement rate of $v_y = 0.3$ m/s was used. The load is transferred to the glass through the contact model introduced in Section 2.2.

3.2. Results and discussion

We first examine the results in terms of fracture patterns and failure load for the simulations with varying bolt-to-end distances. The fracture pattern is exhibited in **Fig. 4** with comparison to experimental observations [37] in **Fig. 5**. The shallow color dots in the model indicates the modeled flaws in the glass. The numerical model is seen to reasonably capture the major features in the fracture pattern for both small and large ratios of *s/d*. For $s/d = 0.75$, the pattern features a vertical fracture in the strip between the hole and the bottom edge and two tilted fractures angled at approximately 30~40 degrees extending from the hole to the bottom edge. For $s/d = 1.0$, similar fracture patterns remain except for the branched cracks that are seen extending to the two sides of the specimen. With larger *s/d* ratios, the vertical crack does not occur. Fractures initiate at the side of the hole and extend to the two side edges, with crack branching observed in some of our other simulations. The findings imply that bolt connections may be placed with bolt-to-end distance greater than 1.5 times the hole diameter to eliminate the bolt-to-end type of failure. As will be shown later, with $s/d \geq 1.5$, the capacity of the glass panel is dependent of the tensile type of fractures extending laterally and is no longer a function of the bolt-to-end distance.

The numerical model allows detailed investigation on the initiation

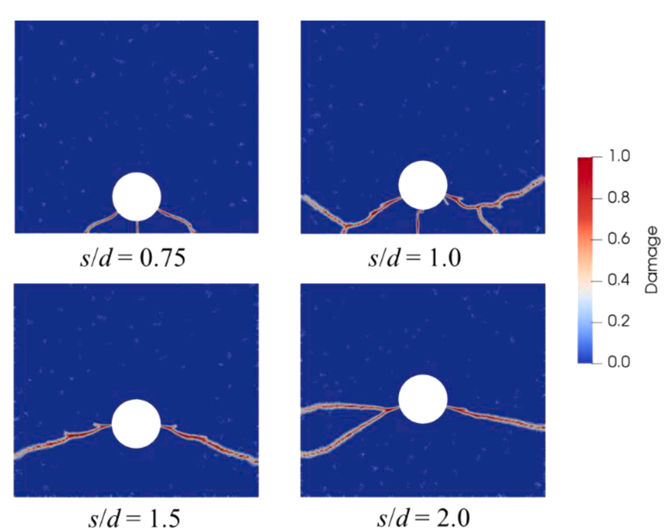

Fig. 4. Fracture patterns of glass with different bolt-to-end distances (the base case and cases *E-1* through *E-3*).

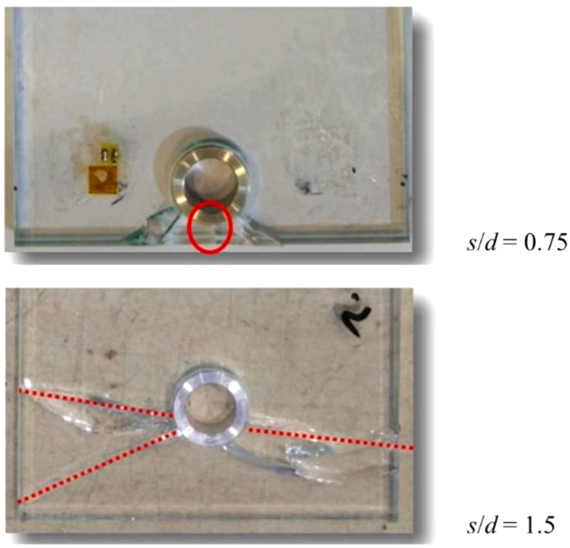

Fig. 5. Experimentally observed fracture patterns for small (top) and large (bottom) ratios of *s/d*.

of fractures which may not be easily identified in experiment without a highspeed camera. Shown in Fig. 6 is the position of fracture initiation recorded in the numerical simulations. The initiation of a fracture is herein defined as the material point that first reaches a damage value of 0.6 or above. Obviously, the fracture initiates near the bottom edge of the specimen when the bolt is positioned close to the bottom edge. With larger ratio of *s/d*, the fractures are most likely to initiate from the two sides of the hole at positions slightly below the centerline.

The evolution of bolt force with the displacement of the metal ring is extracted from a typical model in each of the four cases and is shown in Fig. 7. The bolt force is recorded as the vertical contact force acting on the metal ring. The force-displacement curves show a non-linear pattern at small displacements. The stiffness at the glass-ring contact appears to increase with load application, due likely to the increased contact area. The curves show an approximately linear behavior until failure and the

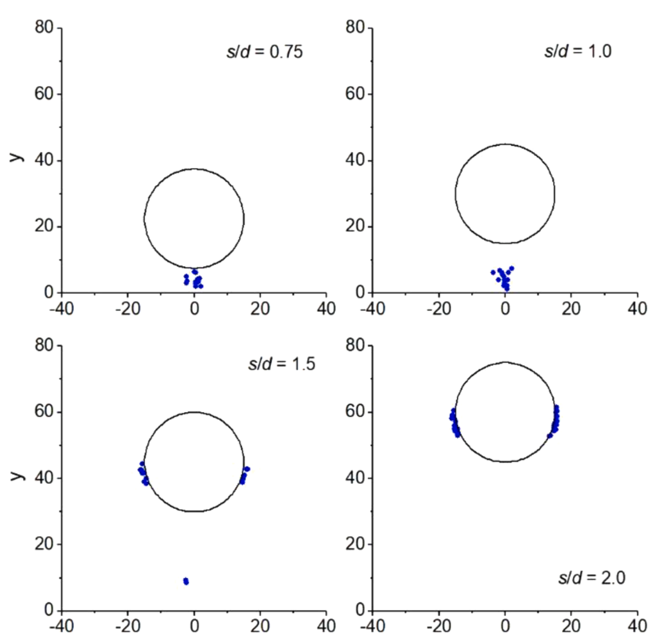

Fig. 6. Location of fracture initiation with different bolt-to-end distances (the base case and cases *E-1* through *E-3*). The circle represents the hole and dot represents the position of fracture initiation.

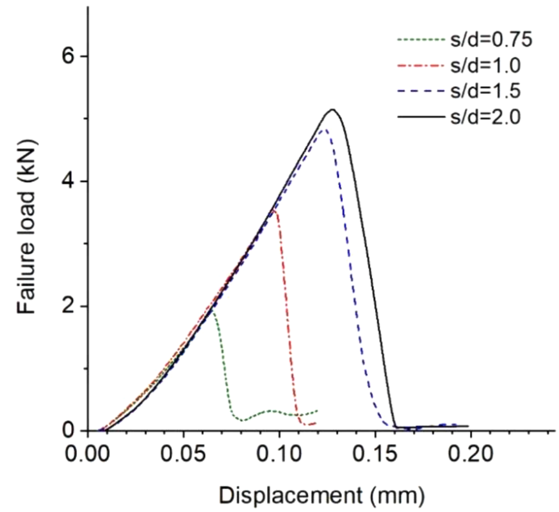

Fig. 7. Bolt force evolution with time for the base case and cases *E-1* through *E-3*.

contact force is lost quickly afterwards. The force level at failure is found to rise with the ratio of *s/d* but such trend is mitigated when *s/d* is greater than 1.5. The observation can be attributed to the change of failure mechanism from cracking the bottom edge to cracking the side edges as shown in Fig. 4. The force levels at failure recorded in all simulations are plotted with their upper and lower bounds as well as the average values in Fig. 8 in comparison with the experimental measurements. The upper and lower bounds of the failure force levels obtained from simulation mostly fall within the range of experiment data, although it appears that the simulation does not capture some of the high strength cases in the experiment. This may be attributed to the assumption made on the edge flaws. If a more dispersed distribution of edge flaw density is used, the strength of the bolt connection would be more dispersed which may offer a better match with the experimental records.

Similarly, for the cases with varying distances between the bolt and side edge (the "*S*" series), the failure loads obtained from the simulation are compared with the experimental measurements in Fig. 9. The predicted failure loads are found within the range of experimental data except for the case with $a/d = 1.0$ where the simulation predicted lower failure forces than those in experiment. For this case, the edge flaws are expected to have a more pronounced influence on the failure of the glass

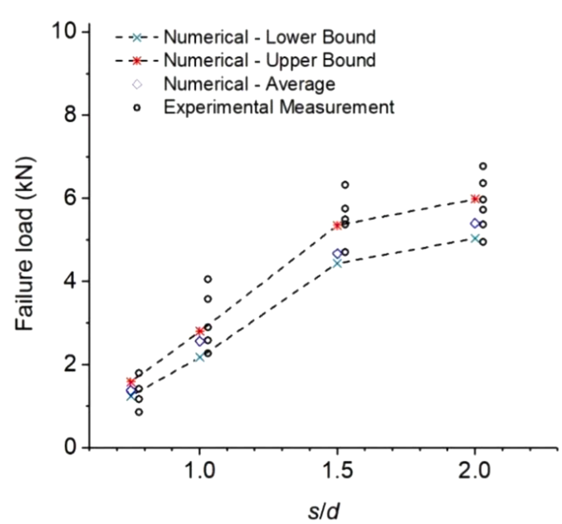

Fig. 8. Failure force levels recorded in simulations for the base case and cases *E-1* through *E-3*. Experimental measurements are also shown in the plots.

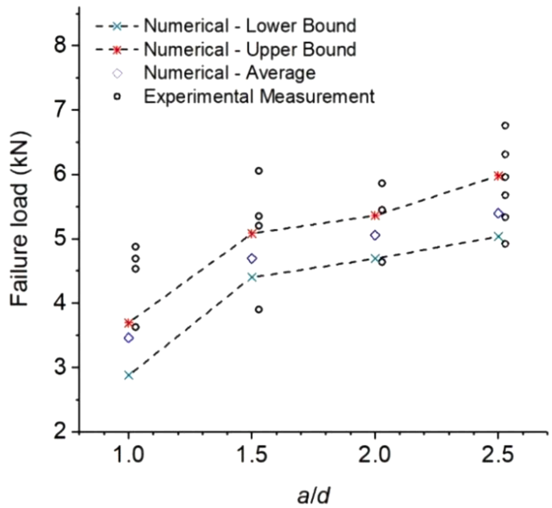

Fig. 9. Failure force levels recorded in simulations for the base case and cases *S-1* through *S-3*. Experimental measurements are also shown in the plots.

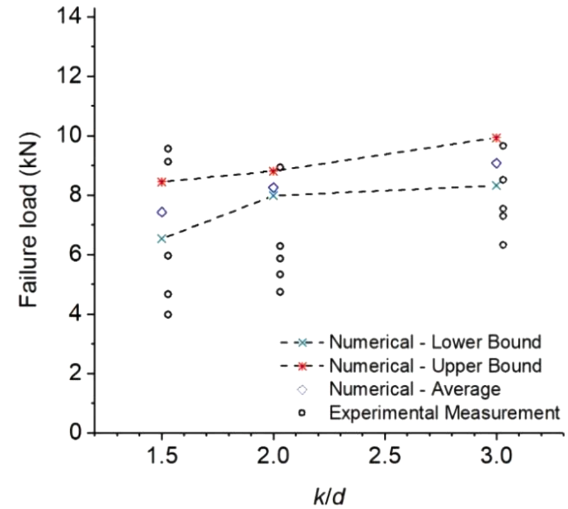

Fig. 11. Failure force levels recorded in simulations for the cases *M-1* through *M-3*. Experimental measurements are also shown in the plots.

since the bolt is close to the edge. The result suggest that the assumed edge flaws are denser and/or weaker than the those in the physical experiment. It can also be noted that larger a/d generally offers higher capacity at the bolt connection. The fracture patterns for the cases *S-1* through *S-3* are exhibited in Fig. 10 together with the experimental records [37]. When $a/d = 1.0$, the fracture pattern is featured by horizonal cracks between the hole and the side edges. For larger a/d ratios, crack branching and tilted fractures were observed in the experiments. Similar features were captured in our simulations.`

For the cases with two bolts (the "*M*" series), the glass strength obtained from simulations are compared with experimental data in Fig. 11, where a reasonable agreement is found. The strength obtained from experiments show an apparent dispersion over a side range for each case. For $k/d = 1.5$ the maximum failure force is more than twice the minimum. This could imply a highly dispersed distribution with respect to the size and/or density of the edge flaws around the holes. It is interesting to note that the numerically predicted glass strengths tend to be slightly lower than what measured. The $k/d = 1.5$ case is selected as a representative case and two representative fracture patterns from simulations and experiments [37] are shown in Fig. 12. The fracture patterns can be rather different even with the same geometry owning to the stochastic distribution of the flaws. As demonstrated in the figure, the

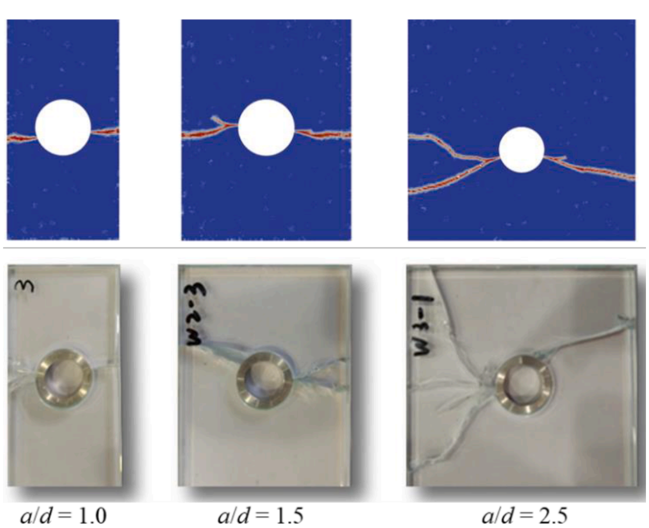

Fig. 10. Fracture patterns for the cases *S-1* through *S-3* from simulation (top) and comparison with experimental observations (bottom).

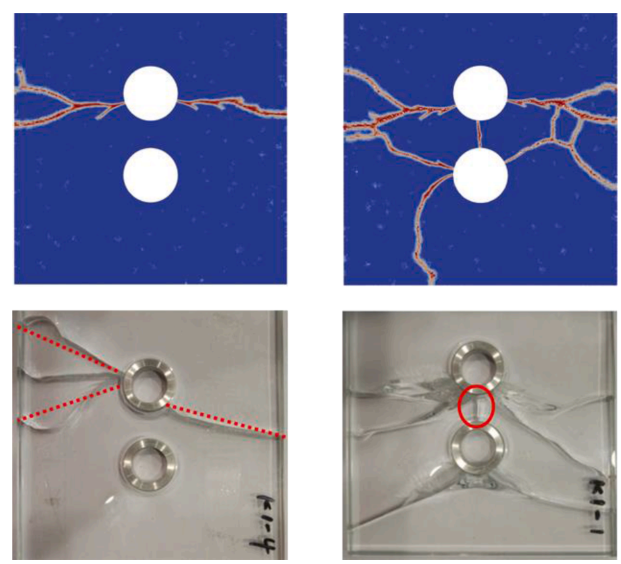

Fig. 12. Fracture patterns for the case *M-1* and comparison with experimental observations.

fracture may propagate from the upper hole to the side edges, with or without branching. Complex fractures connecting the holes were also observed in both the numerical models and experiment. We cannot claim exact match in the fracture patterns since we cannot model the exact flaws that may present in a real glass panel (which affects the trace of fracture path). Meanwhile, other fracture patterns are entirely possible and an exhaustive presentation of those fracture patterns is not pursued here.

We further examine the strength statistics for the base case, where a single bolt is located at $s/d = 2.0$ and $a/d = 2.5$. A total of 200 realizations were analyzed with stochastic distributions of the surface and edge flaws. The results are presented in Fig. 13. Strengths in the range of 4 kN to 6 kN were predicted by the simulations with an average value of 5.3 kN. The data is fitted with both the Weibull distribution and the normal distribution. The Weibull modulus is above 30. The results thus imply a glass material with relatively small variation in strength. In reality, the flaws and particularly the edge flaws at the holes are strongly dependent of the machining procedure used to create them, and therefore this exercise which assumed a mono-sized distribution of edge flaws

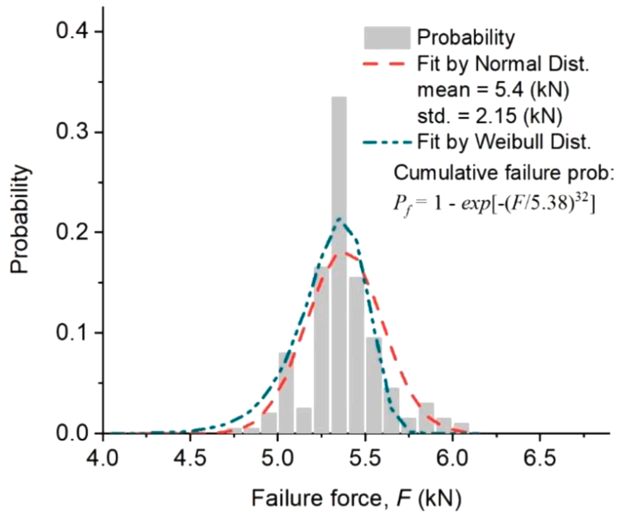

Fig. 13. Glass strength distribution for the base case from 200 simulations.

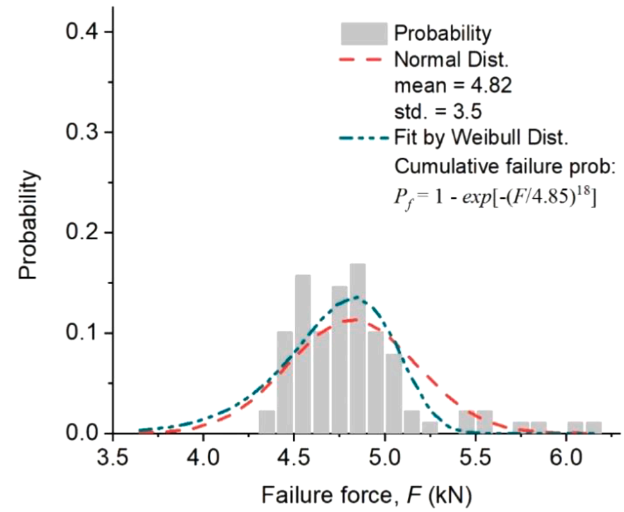

Fig. 14. A parametric study of glass strength distribution for the base case. Hole edge flaws are assumed to be randomly distributed with flaw density ranging from 0.5 to 10 per cm^2 with depth up to 50 μm. Results of 100 simulations.

on the hole surface for all specimens is most likely not realistic. To further examine the influence of flaw assumptions, an extra set of 100 simulations were carried out for the base case, where the edge flaw density is assumed to be randomly distributed among all specimens in the range of 0.5 to 10 per cm^2 with a depth up to 50 μm. Indeed, the resulted strength distribution, as shown in Fig. 14, is more dispersed with a Weibull modulus below 20. The range of strength spans from 4.3 kN to 6.2 kN and is in good agreement with the experimental results in Fig. 8. It is beyond the scope of this work to determine which statistical distribution works best for bolted glass. A faithful model for the glass strength requires a deep understanding of the statistics of micro flaws in glass for which further inputs from experimentalists are needed. The parameters and statistical models for the flaws will be further studied and calibrated in future works.

4. Conclusions and outlook

In this paper, a peridynamic-based computational approach is presented and validated for predicting the strength of bolted glass panels with explicit consideration of the flaws introduced in their production. The ordinary state-based PD theory is employed with a critical stretch failure criterion to describe the elastic brittle failure. A contact model is implemented at the bolt connection. The present study assumes a Pareto distributed single population surface flaws and a mono-sized population of edge flaws. The flaws are explicitly considered in the PD simulations with preset broken material bonds. Simulations are carried out for glass specimens subjected to in-plane loads imposed by single or multi bolts with different geometrical configurations. The predicted failure loads, as well as the fracture patterns, agree reasonably well with the corresponding experiments. The approach is also shown to reflect strength statistics of glass with a series of Monte Carlo simulations. The glass strength distribution is found strongly dependent on the assumptions on the density and size of edge flaws. It is worth mentioning that the PD theory can be applied for modeling fractures of brittle materials under complex loading conditions and failure modes such as blasting [41], impact [42], fatigue [43] where chemical reactions and corrosions may also be considered. The presented study can be further extended to simulate other types of glasses such as laminated glass, aircraft glazing, explosion-proof glass, etc. to suit the need from a broad range of industrial sectors.

Declaration of Competing Interest

The authors declare that they have no known competing financial interests or personal relationships that could have appeared to influence the work reported in this paper.

Acknowledgements

The work was financially supported by the Research Grants Council of Hong Kong through GRF project 16208720.

References

[1] S.M. Wiederhorn, Influence of water vapor on crack propagation in soda-lime glass, J. Am. Ceram. Soc. 50 (8) (1967) 407–414.
[2] E. Orowan, The fatigue of glass under stress, Nature 154 (1944) 341–343.
[3] S.M. Wiederhorn, L.H. Bolz, Stress corrosion and static fatigue of glass, J. Am. Ceram. Soc. 53 (1970) 543–548.
[4] W. Weibull, A statistical theory of the strength of materials, Proc. R. Acad. Engr. Science 15 (1939).
[5] A. Freudenthal, A. Fracture, An Advanced Treatise, 2, Academic Press, New York, 1968.
[6] G. Pisano, G. Royer-Carfagni, A micromechanical derivation of the macroscopic strength statistics for pristine or corroded/abraded foat glass, J. Eur. Ceram. Soc. 37 (2017) 4197–4206.
[7] C. Przybilla, A. Fernández-Canteli, E. Castillo, An iterative method to obtain the specimen-independent three-parameter Weibull distribution of strength from bending tests, Procedia Eng 10 (2011) 1414–1419.
[8] R. Ballarini, G. Pisano, G. Royer-Carfagni, The lower bound for glass strength and its interpretation with generalized Weibull statistics for structural applications, J. Eng. Mech. 142 (12) (2016), 04016100.
[9] C. Klein, Flexural strength of infrared-transmitting window materials: bimodal Weibull statistical analysis, Opt. Eng. 50 (2) (2011), 023402.
[10] F. Veer, C. Louter, F. Bos, The strength of annealed, heatstrengthened and fully tempered float glass, Fatigue Fract. Eng. Mater. Struct. 32 (2009) 18–25.
[11] W.L. Beason, J.R. Morgan, Glass failure prediction model, J. Struct. Eng. 110 (1984) 197–212.
[12] I. Maniatis, Numerical and Experimental Investigations on the Stress Distribution of Bolted Glass Connections Under in-Plane Loads, (Doctoral Dissertation, Technische Universität München), 2006.
[13] K. Sanders, F. Bos, E. ten Brincke, J. Belis, Edge strength of core drilled and waterjet cut holes in architectural glass, Glass Struct Eng 6 (2) (2021) 131–145.
[14] M. Lindqvist, Structural glass strength prediction based on edge flaw characterization, Thesis, EPFL, (2013).
[15] D.T. Kinsella, Modelling of Annealed Glass Fracture. Licentiate Dissertation, Lund University, 2018.
[16] G. Pisano, G. Royer-Carfagni, A micromechanical derivation of the macroscopic strength statistics for pristine or corroded/abraded oat glass, J. Eur. Ceram. Soc. 37 (2017) 4197–4206.
[17] J.R. Matthews, F.A. McClintock, W.J. Shack, Statistical determination of surface flaw density in brittle materials, J. Am. Ceram. Soc. 59 (1976) 304–308.
[18] A. Rufin, D. Samos, R. Bollard, Statistical prediction models for brittle materials, AIAA Journal 22 (0.1) (1984) 135–140.
[19] D.Z. Yankelevsky, Strength Prediction of Annealed Glass Plates - A new model, 79, Eng Struct, 2014, pp. 244–255.

[20] M. Pathirana, N. Lam, S. Perera, L. Zhang, D. Ruan, E. Gad, Risks of failure of annealed glass panels subject to point contact actions, Int. J. Solids Struct. 129 (2017) 177–194.
[21] D.T. Kinsella, K. Persson, A numerical method for analysis of fracture statistics of glass and simulations of a double ring bending test, Glass Struct Eng 3 (2018) 139–152.
[22] S.A. Silling, Reformulation of elasticity theory for discontinuities and long-range forces, J. Mech. Phys. Solids 48 (1) (2000) 175–209.
[23] S.A. Silling, M. Epton, O. Weckner, J. Xu, A. Askari, Peridynamics states and constitutive modeling, J. Elasticity 88 (2) (2007) 151–184.
[24] H. Ren, X. Zhuang, R. Rabczuk, Dual-horizon peridynamics: a stable solution to varying horizons, Comput. Methods Appl. Mech. Engrg. 318 (2017) 762–782.
[25] H. Zhang, P. Qiao, A state-based peridynamic model for quantitative fracture analysis, Int. J. Fract. 211 (2018) 217–235.
[26] H. Zhang, P. Qiao, A two-dimensional ordinary state-based peridynamic model for elastic and fracture analysis, Eng. Fract. Mech. 232 (2020), 107040.
[27] E. Madenci, E. Oterkus, Peridynamic Theory and Its Applications, Springer, New York, NY, USA, 2014.
[28] G. Fang, S. Liu, M. Fu, B. Wang, Z. Wu, J. Liang, A method to couple state-based peridynamics and finite element method for crack propagation problem, Mech. Res. Commun. 95 (2019) 89–95.
[29] F. Zhu, J. Zhao, A peridynamic investigation on crushing of sand particles, Géotechnique 69 (6) (2019) 526–540.
[30] P.K. Jha, P.S. Desai, B. Debdeep, R. Lipton, Peridynamics-based discrete element method (PeriDEM) model of granular systems involving breakage of arbitrarily shaped particles, J. Mech. Phys. Solids 151 (2021), 104376.
[31] D. Kamensky, M. Behzadinasab, J.T. Foster, Y. Bazilevs, Peridynamic modeling of frictional contact, J. Peridyn. Nonlocal. Model 1 (2019) 107–121.
[32] A. Jayatilaka, K. Trustrum, Statistical approach to brittle fracture, J. Mater. Sci. 12 (1977) 1426–1430.
[33] J.D. Poloniecki, T.R. Wilshaw, Determination of surface crack size densities in glass, Nat. Phys. Sci. 229 (1971) 226–227.
[34] J. Poloniecki, Statistical Investigation of Surface Flaws, The University of Sussex, 1974. PhD Thesis.
[35] A. Wereszczak, M. Ferber, W. Musselwhite, Method for identifying and mapping flaw size distributions on glass surfaces for predicting mechanical response, Int. J. Appl. Glass Sci. 5 (2014) 16–21.
[36] F. Zhu, J. Zhao, Multiscale modeling of continuous crushing of granular media: the role of grain microstructure, Comp. Part. Mech. 8 (2021) 1089–1101.
[37] S. Peng, Study on Static Mechanical Properties of Bold Connections in Glass Structures, MEng dissertation, Tongji University, 2018.
[38] E. Le Bourhis, Glass, Wiley-VCH Verlag GmbH & Co KGaA, Weinheim, 2008.
[39] Q.V. Le, F. Bobaru, Surface corrections for peridynamic models in elasticity and fracture, Comput. Mech. 61 (2018) 499–518.
[40] C. Geuzaine, J.F. Remacle, Gmsh: a three-dimensional finite element mesh generator with built-in pre- and post-processing facilities, Int. J. Numer. Methods Eng. 79 (11) (2009) 1309–1331.
[41] F. Zhu, J. Zhao, Peridynamic modelling of blasting induced rock fractures, J. Mech. Phys. Solids 153 (2021), 104469.
[42] X. Lai, B. Ren, H. Fan, S. Li, C.T. Wu, R.A. Regueiro, L. Liu, Peridynamics simulations of geomaterial fragmentation by impulse loads, Int. J. Numer. Anal. Methods Geomech. 39 (12) (2015) 1304–1330.
[43] G. Zhang, Q. Le, A. Loghin, A. Subramaniyan, F. Bobaru, Validation of a peridynamic model for fatigue cracking, Eng. Fract. Mech. 162 (2016) 76–94.